Numerical Capture and Validation of a Massively Separated Bluff-Body Wake

K. J. B. Tan* and H. Hesse†
University of Glasgow Singapore, Singapore 599493

P. C. Wang‡
Singapore Institute of Technology, Singapore 138683

A flow over a bluff-body is numerically investigated and validated using a Detached-Eddy Simulation (DES) technique at Re=21,400. An incompressible solver that is nominally second-order accurate employing an implicit constant backward time-stepping scheme with blended upwind-central differencing spatial discretization is used to study the massively separated wake that is generated. Measurements are taken up to 6 downstream characteristic lengths, evaluating the wake time-averaged first- and second-moment statistics alongside near-wall boundary layer quantities and surface-force integrals. Results advocate the use of DES methods, which are found to be significantly more accurate for capturing wake statistics, compared to two different Reynolds-Averaged (RANS) models calibrated with an identical grid. Although comparative accuracy can be obtained with the RANS techniques for the boundary layer and surface-forces, these techniques are unsuitable for modeling wake statistics as they are inherently dissipative, evident through early velocity recovery when evaluated against experimental data.

I. Introduction

Wake phenomena and its encounter with nearby bodies are of engineering importance as these can affect aerodynamic loads. This is critical, as flows over obstacles can produce wakes of aerodynamic significance to bodies in proximity. These interactions concern a variety of engineering disciplines; such as the aerodynamics among building clusters due to the convection of natural wind [1], the handling qualities and flight simluation of rotorcraft encountering building or ships wakes [2, 3], or even the controls for unmanned aerial vehicles under the influence of wind conditions induced by urban environments [4–6]. These examples demonstrate that the effects of a wake encounter emanated from nearby sources can induce unfavorable—or even dangerous—conditions to aerodynamics and affects engineering design. Wake encounters are a critical design consideration, and a high-fidelity simulation model that captures these wake physics of interest accurately is required to predict any induced behaviors. Accurate capture of wake physics and vortex shedding behavior is therefore a precursor that forms the foundation to modeling of consequent loads due to wake interactions.

As a myriad of possible geometry configurations can be responsible for a wake generator, the square beam bluff-body ("square cylinder") has been a long-standing benchmark geometry [7] for the validation of Computational Fluid Dynamics (CFD) methods with experiments [8]. Although the geometry may be relatively simple, complex flow phenomena can exist throughout flow regimes over the square beam. At lower, near laminar speeds ($Re \approx 100$), it has been observed that flow separation does not necessarily occur at the leading edges but remains attached on the surface of the geometry for half its width [9, 10]. At these slower and transitional regimes, several modes of flow invloving the transition from laminar flow to the alternating von Kármán sheet across $50 < Re < 160$ can also be observed. This mode occurs through the shedding of shear-layer instabilities over the leading edges and their transition to turbulence, where vortex shedding with wake dynamics become prevalent [11, 12]. The evolution of time-averaged drag and Strouhal number as the flow becomes transitional also behaves asymptotically at higher ($Re > 1.0 \times 10^4$) Reynolds numbers [9].

As a wide range of flow phenomena is expected ranging from near-wall flow developments, to vortex shedding and wake dynamics, numerical methods have the flexibility for entire domains to be discretised and measured freely, without interference from the necessary physical apparatus required in experiments. In addition, the geometry favours the generation of orthogonal grids for turbulence modelling and validation. However, general purpose RANS techniques based on the Boussinesq hypothesis for eddy-viscosity dampens convection begin to exhibit non-physical dissipating

*Postgraduate Research Student, Aerospace Division, AIAA Student Member.
†Assistant Professor, Aerospace Division, AIAA Member.
‡Assistant Professor, Engineering Cluster.

behaviours even for attached flow regimes. This is observed to occur as close as two characteristic lengths downstream [13, 14]. As bodies of interest can be located beyond this [2, 3], accurate capture of wake physics at these distances may be unsuitable for these techniques. This inadequacy can be further exacerbated under massively separated conditions, despite good accuracy for surface force integrals. However, large-scale full- and half-loop vortex structures at transitional Reynolds numbers could still be distinguished in the wake of a finite ($AR = 7$) cuboid [15]. Key quadrupole and dipole wake structures were qualitatively identified in this transitional regime ($652 < Re < 13\,041$) with Reynolds Stress Models. In addition, findings on the asymptotic behaviour in the drag coefficient at Reynolds number range also agree with other studies [9].

At higher Reynolds numbers ($Re > 1.0 \times 10^4$), the wake shed by a bluff body can be described by several characteristic quantities. Benchmark conditions [8, 16–21] at $Re = 21\,400$ showed that the time-averaged drag coefficient ranges approximately 2.1 to 2.4, with Strouhal numbers ranging 0.12 to 1.4. This shedding frequency is correlated to the vortex shedding pair that forms due to the roll-up of the shear-layer instabilities at the leading edges. Along the wake centre, it is observed that a region of lower pressure and recirculation zone exists leeward of the geometry. As the momentum of the fluid recovers, a recirculation distance in the order of x/D where the local velocity at a point along this wake centre can be found to stagnate. Past this, the width of the wake grows, and the time-averaged (first-moment statistics) of wake centre velocity recovers towards the freestream. Some studies have also extended beyond the focus of bluff-bodies to compare vortex shedding behaviours with streamlined shapes. At flow separating attitudes without boundary layer reattachment, the shedding characteristics for symmetrical airfoils can resemble those typical of bluff-body wakes—although the Strouhal numbers of streamlined bodies are more sensitive to changes in Reynolds numbers at lower ($\leq 10°$) angles of attack [22]. At post-stall (15° to 90°), it is observed that the Strouhal number tends to remain constant beyond $Re_c > 2.5 \times 10^4$, which is similar in magnitude observed for the square beam [9, 23]. The dominant frequencies in the wake spectra have Strouhal numbers ranging from 0.12 to 0.22, which coincides with those observable from bluff-bodies. However for streamlined bodies, a broader spectrum of frequencies can be observed within the wake spectra due to the shear-layers emanated from the asymmetry with respect to the flow direction caused by the leading and trailing edges [23, 24].

More importantly, fluctuating quantities become increasingly dominant at these turbulent regimes. As they are of engineering importance, Unsteady-RANS (URANS) methods become unsuitable as fluctuations can be lost through the process of Reynolds decomposition ($\phi_i = \overline{\Phi_i} + \phi_i'$). Wake behaviour can therefore become numerically damped, which is attributed to an excess of turbulent viscosity production [16]. LES techniques are among those that have been increasingly used for resolving the turbulent flows [17, 18]. Mean moment statistics along the wake centre have been captured using Scale Adaptive Simulations (SAS) [19], and one-equation dynamic models provided good agreement in terms of the root-mean-square velocities [17], evaluated against laser-Doppler measurements [8]. Near the walls, it is suggested that the capture of near-wall features are key as shear layer (Kelvin-Helmholtz) instabilities at the points of separation are propagated downstream into the von Kármán sheet [20]. However, turbulent length scales approach the order of the boundary layer thickness near the wall and LES depends on the filter width, with a sub-grid scale spacing ($\phi_i = \hat{\Phi}_i + \phi_i^{SGS}$) that can be limited towards DNS levels [21]. This can become unnecessarily computationally expensive in terms of wall grid resolution, especially for practical purposes.

However, advancements in turbulence modelling towards hybrid methods have alleviated such demands with a hybrid length scale definition where a RANS solution is confined to the boundary layer region, with an LES-like activation farther from the walls [25]. Hybrid RANS-LES methods therefore provide a good compromise between RANS and LES techniques [26, 27]. The evaluation of DDES (Delayed Detached-Eddy Simulation) capabilities determined that the accuracy of the wake statistics increases with refinement of the subgrid-scale definition [28]. The grid sensitivity study was performed on refinement sizes in the order of $\Delta/D = [0.03, 0.05, 0.1]$ with agreeing results compared to pre-existing experimental data [8] were performed on a finer ($0.03\Delta y/D$) grid coupled with a modified Total Variation Diminishing scheme. However, the two coarser $\Delta y/D = [0.05, 0.1]$ refinement grids produced similar results, with an approximate $0.1\overline{U}/U_\infty$ over-prediction in wake velocity recovery. A similar $0.05\Delta/D$ grid resolution in the wake was also used with spatial (upwind-based) schemes that are second-order accurate, although with comparatively slightly better results [16]. Both examples successfully employed the hybrid method, by demonstrating reasonable accuracy in representing the time-averaged velocity recovery and its root-mean-square statistics for the wake centre.

The objective of this paper focuses on the applied numerical methodologies for a canonical study of a wake generator represented with a flow encountering a square beam bluff-body. Vortex shedding dynamics and wake physics are simulated using the OpenFOAM CFD C++ toolkit, where the solvers validity and accuracy of the wake simulated is evaluated against pre-existing experimental benchmark data. The extent of wake capture is first validated at the source, where the suitability of the near-wall grid design is assessed to ensure adequate boundary layer and wall surface

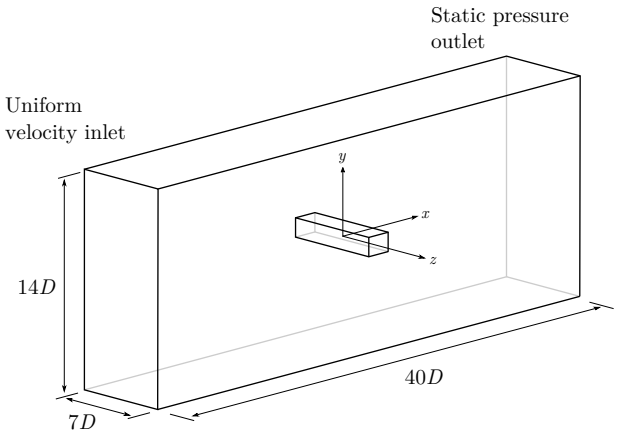

Fig. 1 The square beam simulation domain.

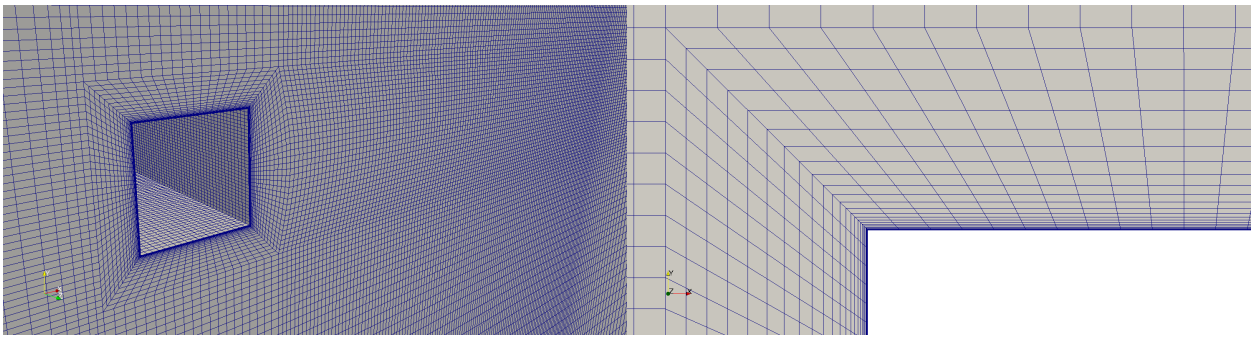

(a) Computational domain with wake refinement block **(b) Wall grid design, $y^+ < 1$**

Fig. 2 A structured O-H-grid topology with a block (H-grid) downstream used for cell refinement in the wake region.

treatment. This translates to the time-averaged and fluctuating first- and second-moment statistics of lift and drag surface-force coefficients. The frequency spectra of these forces also detail characteristics between their shedding behaviours. Moving downstream, the wake centre and cross-stream profiles are measured up to $6x/D$, where coherent vortex structures are identified as part of the von Kármán sheet. The formation of these structures are emanated from the leading edges as shear-layer instabilities which roll-up and stretch into these larger, coherent vortex structures. The work further distinguishes itself by establishing the extent of turbulent wake treatment with both DES and RANS methods where the former agrees well to published results performed with LES and DNS methods [17, 20, 21]. Here, the expected inherent dissipating characteristics of the RANS solutions also become evident, and are demonstrated through its eddy viscosity ratio in the wake.

II. Simulation Methodology for Wake Capture

The wall mounted Square Beam (SB) of characteristic length, D, with infinite span is placed adjacent to the horizontal oncoming flow. The side boundaries of the domain spans $7D$ ($AR = 7$) across, with the inlet and outlet spaced $40D$ apart. The top and bottom boundaries are spaced at $14D$ with the geometry located at the centroid of this domain. These are based on a Cartesian coordinate system where the positive x direction is aligned with the flow, as illustrated in Fig. 1.

A. Grid Description

An O-H-grid topology composed of 15 hexagonal blocks discretizes the fluid domain for the geometry as illustrated in Fig. 2. The O-grid surrounds the beam at a distance of $0.3D$ from the surface for the boundary layer grid, where the

Table 1 Summary of grid statistics.

Topology	Blocks	y^+	Layers	Growth, δ	Δ_{wake}
Hex, Structured, O-H	15	< 1	25	1.10	0.05D

first cell height resides within the viscous sub-layer at $y^+ < 1$. This first cell stretches at a cell growth rate of 1.1 over 25 layers. The $\Delta x, z$ cell widths are also maintained at $0.05D$, which transfers along parallel block edges for cell isotropy in the wake block located downstream. The highest aspect ratio among cells which are at the wall are in the order of 100. Downstream, a single block is used for wake refinement, and extends up to $7x/D$ from the geometry origin at its centroid. The grid then expands to the far field regions of the domain boundaries. With this grid design, the entire computational domain comprises of approximately 4.1×10^6 elements. In terms of quality, the grid has a maximum non-orthogonality of 47°, which occurs along the four leading and trailing edges of the geometry. Because of the high orthogonality among all other cells, mostly in the volume of the wake block, the overall non-orthogonality quality of the grid is strong which averages to 7°.

B. Governing Equations and Numerical Schemes

Flow conditions are at $Re = 2.14 \times 10^4$, with reference to standard sea-level conditions, assuming fully turbulent, incompressible, isothermal conditions of the Navier-Stokes (continuity and momentum) equations where:

$$\frac{\partial u_i}{\partial x_i} = 0, \tag{1a}$$

$$\frac{\partial u_i}{\partial t} + u_j \frac{\partial u_i}{\partial x_j} = -\frac{1}{\rho}\frac{\partial p}{\partial x_i} + \nu \frac{\partial^2 u_i}{\partial x_j \partial x_j}, \tag{1b}$$

The equations in the general form are discretised with schemes that are nominally second-order accurate. Spatially, the divergence terms are discretised with a blended central-upwind differencing scheme (CD-UD) [29]:

$$\phi_f = (1-\gamma)(\phi_f)_{UD} + \gamma(\phi_f)_{CD}, \tag{2}$$

where discretisation of the arbitrary primitive variable ϕ is blended with the coefficient γ, weighted at 0.75. As boundedness is not guaranteed with central differencing, an upwind-blended scheme provides boundedness resulting in better numerical stability and accuracy. Time discretisation is achieved with a second-order implicit, backward-differencing scheme [30], where:

$$\frac{\partial \phi}{\partial t} = \frac{\frac{3}{2}\phi^n - 2\phi^o + \frac{1}{2}\phi^{oo}}{\Delta t} \tag{3}$$

A segregated approach is taken where the pressure-velocity coupling for the time-marching solution is achieved with the PISO (Pressure-Implicit with Splitting Operators) algorithm. The *semi*-discretised form of the momentum equations are then $a_p \mathbf{U}_p = \mathbf{H}(\mathbf{U}) - \nabla p$, where a_p and $\mathbf{H}(\mathbf{U})$ are the diagonal and the off-diagonal (convective and diffusive) coefficient matrices, respectively. A constant time-step selection that is adequately fine ensures that the algorithm is conditionally stable with diagonal dominance. This is based on the maximum Courant number in the domain, by referencing the smallest cell sizes with highest relative local velocities due to the shear layer instabilities that are located over the leading edges of the geometry. Under these conditions, the wake $C_o \approx 0.2$, and translates to $\Delta t_c = 6.25 \times 10^{-3}$ which satisfies the Courant–Friedrichs–Lewy condition [31].

For time-averaging, the solution time-history is limited towards a sufficiently large instance relative to fluctuations to ensure that the statistical average (mean) is sufficiently sampled to be insensitive to the amount of time samples taken. After allowing a flow development phase of approximately 50 characteristic lengths, a subsequent sample size of 250 is sampled for the URANS case. Due to the turbulent extent of the DDES solution, this sample size is further increased to 950. Table 2 summarises and compares the case parameters alongside the existing studies.

Table 2 Case comparisons of wake block grid cell size, characteristic time step, Courant number, and time-history sample size for the Square Beam (SB) case.

Cases	Type	$Re \times 10^3$	Δ_{wake}, D	$\Delta t_c \times 10^{-3}$	Co	T
SB	URANS (DDES)	21.4	0.05	6.25 (3.125)	0.2[†]	250 (950)
Boudreau et al. [16]	URANS (DDES)	21.4	0.05	10	0.2	209.5 (1507.5)
Barone and Roy [28]	DES	19.4	0.095-0.032	3.2	-	250.8[*]
Sohankar et al. [17]	LES	22.0	0.1-0.16	12.5	-	-
Fureby et al. [18]	LES	21.4	-	-	0.5[‡]	-
Trias et al. [21]	DNS	22.0	-	0.97 & 1.71	-	605

[†] Relative to local wake cell size.
[*] Average of three reported cases.
[‡] A reported domain maximum.

C. Turbulence Modelling

The Spalart-Allmaras (SA) one-equation turbulence model solves for a single transport quantity given by:

$$\underbrace{\frac{\partial \tilde{\nu}}{\partial t} + \frac{\partial (\tilde{\nu} u_j)}{\partial x_j}}_{\text{Convection}} = \underbrace{c_{b1}\tilde{\nu}\tilde{S}}_{\text{Production}} \underbrace{- c_{w1} f_w \left(\frac{\tilde{\nu}}{d}\right)^2}_{\text{Destruction}} + \underbrace{\frac{1}{\sigma}\frac{\partial}{\partial x_k}\left[(\nu + \tilde{\nu})\frac{\tilde{\nu}}{\partial x_k}\right] + \frac{c_{b2}}{\sigma}\frac{\partial \tilde{\nu}}{\partial x_k}\frac{\partial \tilde{\nu}}{\partial x_k}}_{\text{Diffusion}} \tag{4}$$

this is related to turbulent viscosity through:

$$\nu_t = \tilde{\nu} f_{\nu 1}, \qquad f_{\nu 1} = \frac{X^3}{X^3 + C_{\nu 1}^3} \tag{5}$$

The variant used here excludes the f_{t2} trip term, calibrated with the model coefficients that are as recommended by the source [32, 33]. Being a one-equation model, it neglects turbulent kinetic energy in the Boussinesq hypothesis for Reynolds stresses where:

$$-\rho\overline{u_i' u_j'} = 2\mu_t \overline{S}_{ij} - \frac{2}{3}\rho k \delta_{ij}, \tag{6}$$

becasue of this its performance can therefore be impeded especially for the modelling of massively separated flows or those with adverse pressure gradients such as in this case.

The second RANS model that is considered is the k-ω SST model that based on two-equations for the transport of turbulent kinetic energy and specific dissipation rate. It is also highly regarded [14] which offers a blend between the standard k-ω and k-ϵ models [34, 35]. The additional equation obtains turbulence intensity, which in contrast to the one-equation model, addresses turbulent kinetic energy in the Boussinesq hypothesis. The transport equations for turbulence kinetic energy and specific dissipation rate are given by:

$$\frac{\partial k}{\partial t} + u_j \frac{\partial k}{\partial x_j} = P_k - \beta^* k\omega + \frac{\partial}{x_j}\left[(\nu + \sigma_k \nu_t)\frac{\partial k}{\partial x_j}\right] \tag{7a}$$

$$\frac{\partial \omega}{\partial t} + u_j \frac{\partial \omega}{\partial x_j} = \alpha S^2 - \beta\omega^2 + \frac{\partial}{\partial x_j}\left[(\nu + \sigma_\omega \nu_t)\frac{\partial \omega}{\partial x_j}\right] + 2(1 - F_1)\sigma_{\omega^2}\frac{1}{\omega}\frac{\partial k}{\partial x_i}\frac{\partial \omega}{\partial x_i} \tag{7b}$$

where F_1 is the blending function that distinguishes the definition between the boundary layer and the freestream, and all model constants and sub-functions are taken as given by the source [34].

The DES formulation is built upon the SA model that is based on the correlation of its production ($c_{b1}\tilde{\nu}\tilde{S}$) and destruction ($c_{w1} f_w(\tilde{\nu}/d)$) terms in its transport equation [26]. Balancing these terms gives a relationship that scales the eddy-viscosity with the local deformation rate and distance to the wall. This is analogous to the Smagorinsky model where it scales with its sub-grid scale eddy-viscosity and grid spacing instead. With this, the distance to the wall in the original SA model is replaced with a hybrid length scale:

$$\tilde{d} \equiv d - f_d \max(0, d - C_{DES}\Delta), \tag{8a}$$

Table 3 Summary of boundary conditions for the computational domain.

Boundary	Type	Velocity	Kinematic pressure
Inlet	Inflow	$u_i = U_\infty$	$\partial p/\partial n = 0$
Outlet	Outflow	$\partial u_i/\partial n = 0$	p = 0
Far fields	-	$\partial u_i/\partial n = u_i \cdot \hat{n} = 0$	$\partial p/\partial n = p \cdot \hat{n} = 0$
Walls	No-slip	$u_i = 0$	$\partial p/\partial n = 0$

where:

$$f_d \equiv 1 - \tanh([8r_d]^3), \qquad r_d \equiv \frac{\nu_t + \nu}{\sqrt{U_{ij}U_{ij}}k^2d^2}, \tag{8b}$$

and $f_d = 0$ yields RANS and LES modes for the hybrid length scale. The C_{DES} constant is calibrated to 0.65. This hybrid formulation allows a RANS-like behaviour and a Smagorinsky-like LES model that switches depending on the proportions between the distance to the wall and local grid spacing. The sub-variant used here is the Delayed-DES (DDES) model which provides an adjustment to the definition of the hybrid length scale that narrows the region of uncertainty between RANS and LES modes. This improved variant has been demonstrated to perform more accurately for massively separated flows [26].

D. Boundary and Initial Conditions

The solution domain is velocity-driven, with a freestream inlet and a static pressure outlet. No-slip boundary conditions are imposed on the walls with all remaining far field boundaries taken to be of zero flux and normal components. Computation of turbulent viscosity, ν_t, is constrained with a turbulent viscosity ratio of $\nu_{t_\infty}/\nu_\infty = 0.01$. The turbulent viscosity for the inlet is determined using kinematic viscosity, $\nu = \mu/\rho$. For the SA model, the modified eddy-viscosity term, $\tilde{\nu}$, where $\tilde{\nu}_\infty = 5\nu_\infty$ for fully turbulent flows, and at the walls, $\nu_{t_{wall}} = \nu_{wall} = 0$ is used. The k-ω SST model introduces two additional terms, which are the turbulent kinetic energy, k, and specific dissipation, ω. The inlet values reference the freestream based on turbulent intensity where $k_{inlet} = 3/2(U_\infty I)^2$, taking $I = 0.01$, and specific dissipation, $\nu_t = k/\omega$. For no-slip conditions, the turbulent kinetic energy, $k_{wall} = 0$.

The grid is initially calibrated for grid independence with the SA model assuming steady flow conditions. The internal fields from this steady solution is then subsequently used for the initialisation of the time-marching transient calculations. The URANS solution is used for the initialisation of the DDES case where a development time of 50 convective time-steps is used for the solution to adjust to the updated turbulence model. These numerical solutions are achieved through pisoFoam solver in the OpenFOAM library [36, 37].

III. Turbulent Wake Capture Shed by a Bluff Body

A. Evaluation of Boundary Layer Grid

The near-wall grid is assessed independently as an extract of the top surface grid settings described in Table 1 under identical flow conditions. A fully developed boundary layer over this distance is achieved with a cyclic inlet-outlet interface where evaluation with the Law of the Wall is valid [38]. The dimensionless velocity is obtained as:

$$y^+ = \frac{yu_\tau}{\nu}, \qquad u^+ = \frac{u}{u_\tau}, \tag{9}$$

where:

$$u_\tau = \sqrt{\frac{\tau_w}{\rho}}, \qquad \tau_w = \mu\left(\frac{\partial u}{\partial y}\right)_{y=0} \tag{10}$$

Discrete points in Fig. 3 represent cell-centred values. Based on this boundary layer grid design, six cell centres reside well within the viscous sub-layer at $y^+ < 5$. The same grid is run with the k-ω SST model and compares well against the SA results, and other numerical studies [32] with comparable flow conditions ($Re = 1.0 \times 10^4$). The cyclic flow conditions for the present grid assumes attached flow but the formation of a separation zone over the leading edges of the geometry would induce much lower local velocities over the upper and lower surfaces as seen in Fig. 4. The

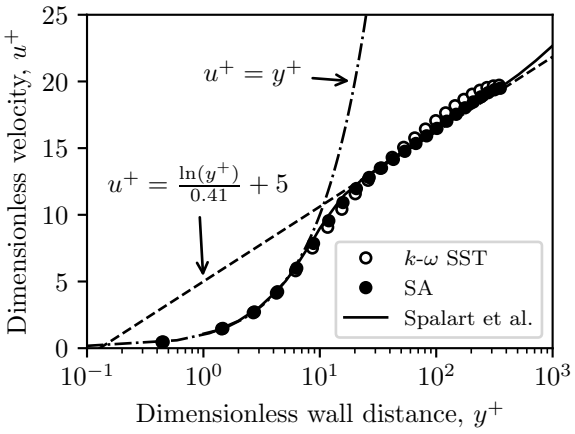

Fig. 3 Evaluation of wall grid design with Law of the Wall [38] and data from Spalart et al. [32].

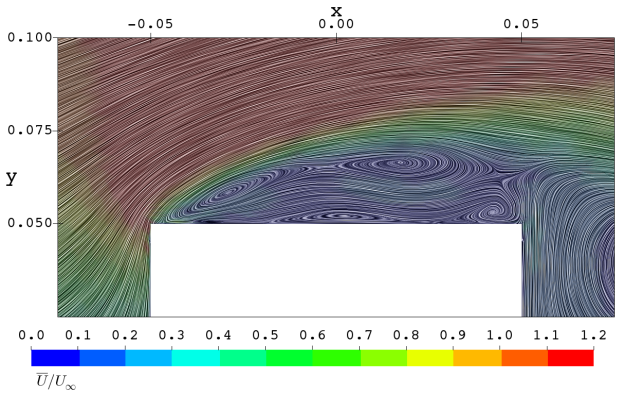

Fig. 4 Time-averaged normalised velocity magnitude contoured with line integral convolution, showing leading edge separation.

time-averaged surface line integral convolution illustrates the leading edge separation vortices over the extend of the characteristic width of the geometry. This is expected to result in a $y^+ < 1$ for the full case due to boundary layer recirculation with lower local velocities. This result demonstrates adequate grid design for capturing boundary layer effects.

B. Vortex Shedding Dynamics and Surface Integral Statistics

Vortex shedding dynamics is made apparent through instantaneous contours of the von Kármán street as illustrated for the three cases in Fig. 5. Coherent three-dimensional flow structures are identified with iso-surfaces of wake vortices identified with the λ_2-criterion [39] based on the eigenvalues of symmetric and anti-symmetric parts ($\mathbf{S}^2 + \mathbf{\Omega}^2$) of the velocity gradient tensor ($\mathbf{J} = \nabla\vec{U}$) contoured with instantaneous velocity. Based on the contours, the DDES solution is capable of capturing and identifying a greater resolution of smaller-scale vortex structures in comparison to the URANS cases. The shear-layers emanated from the leading edges are convected downstream that eventually roll-up and stretch into a larger coherent span-wise vortex structures trailing the geometry. This is observable for all cases but the DDES solution distinguishes itself with much greater flow details.

The drag coefficient frequency oscillates at approximately *twice* that of lift based on Discrete Fourier Transform with the analyses as shown in Fig. 6. These are at 4.37 and 8.91 Hz for the SA results (Fig. 6a) and overall observations for all three cases agree with the von Kármán street dynamics as these parallel and perpendicular forces persist in cross-flow directions [38]. This relationship is easily distinguishable for the SA and k-ω SST cases in their frequency domains (Figs. 6a and 6b) but not as apparent for the DDES case, which is only revealed in its power spectra (Fig. 6c). Both peak dominant frequencies for the URANS cases agree at approximately 4.3 Hz, whereas results from the DDES are relatively higher by approximately 2 %. Using this frequency, a period of 0.225 s for the DDES case can be obtained and reveals a resolution of 1126 time-steps per wave period. Despite the significant similarities between the models in the frequency domain, their differences become apparent in the (log-log) power spectra, which shows that the hybrid solution can capture more information compared against the eddy-viscosity solutions.

The results for dominant frequencies in Fig. 6 corresponds to a Strouhal number of 0.140 and 0.142 for the SA and DDES solutions, respectively. This amounts to a difference of 1.43 % between the two techniques, but is over-predicted by 7.58 % with respect to the experimental data [8]. Table 4 summarises these surface-integral statistics against other comparable benchmarks of the same square beam geometry. Metrics are mainly based on the time-averaged lift and drag coefficients alongside root-mean-square statistics of their respective signals. The obtained drag coefficient has a good agreement with the benchmarks, accurate to a 100-count precision. Another parameter captured is shown in Fig. 7 that demonstrates the extent of the trailing recirculation zone aft of the geometry. The mean recirculation length of the wake is also captured with a 5% error relative to the experiment [8] by taking the closest stagnation point along the time-averaged wake centre. This difference accounts for the precision of the discrete measurement to the closest cell-centre. In comparison, the DDES results under-predicts this length by less than 5 % relative to the experiment and other numerical work [8, 20].

To investigate the difference in Strouhal numbers, it was reported that a two-component Laser-Doppler Velocimetry along the wake is used for monitoring velocity fluctuations [8]. Identical locations along this centre ($x/D = [1, 2, 3, 6]$) are similarly probed for their point vertical velocity component and the dominant frequencies at these locations coincides with lift at approximately 4.44 Hz. Further investigation for sensitivity with regards to time discretisation by halving the time-step size also reveals no appreciable difference in the Strouhal number. Other work (Table 4) also lists numerical cases that are corrected for blockage effects. This correction factor is applied to confined (ducted) spaces and non-slip far field boundary conditions [17, 28]. However, blockage corrections should not apply considering the far field boundary conditions for the present case as this does not lead to an increase in dynamic pressure across the domain. Despite the over-prediction in Strouhal number relative to the experimental cases, the key results obtained are consistent with other numerical cases for time-averaged drag prediction, Strouhal number, and mean recirculation length [18, 20, 21].

C. First- and Second-Moment Wake Statistics

The DDES solution provides a significantly greater amount of information comparing the instantaneous velocity magnitude and span-wise vorticity component contours in Figs. 8 and 9. The results from both the SA and k-ω SST solutions appear to convey the same degree of information in the instantaneous contours and therefore only that from the SA solution is presented. Finer flow details are easily observable through the velocity contours (Fig. 8) and the amount of mixing downstream, convected from the upper and lower shear-layers over the leading edges of the bluff-body is evident in Fig. 9b. The significant loss of information through the process of Reynolds decomposition reduces the

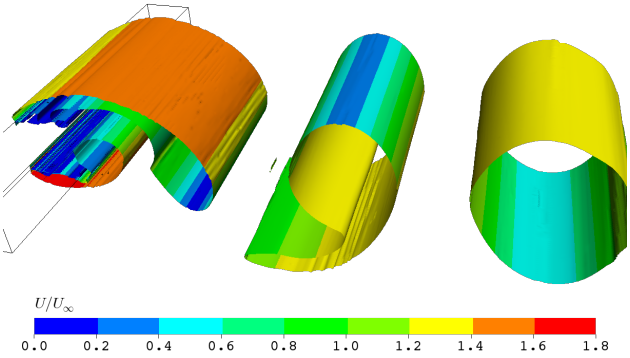

(a) SA

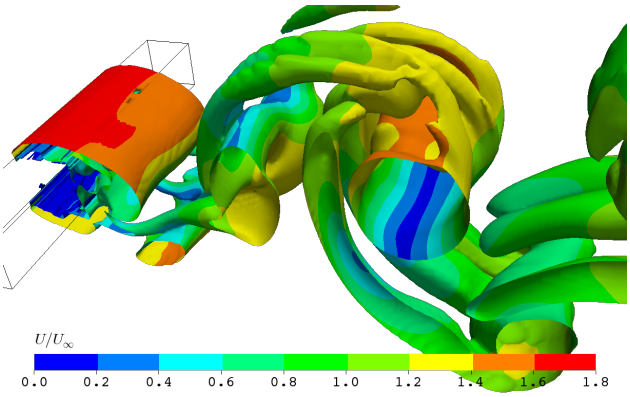

(b) k-ω SST

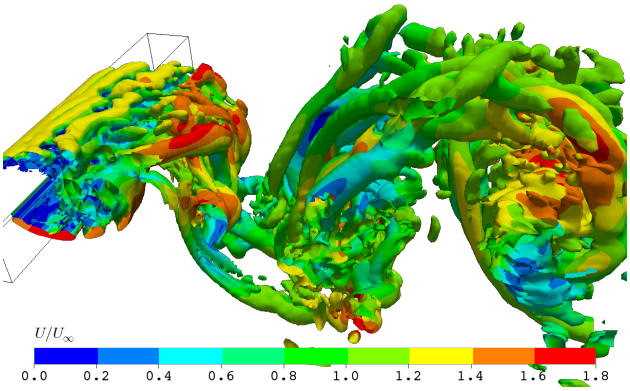

(c) DDES

Fig. 5 Instantaneous vortical structures identified with λ_2-criterion iso-surfaces contoured with normalised velocity magnitude.

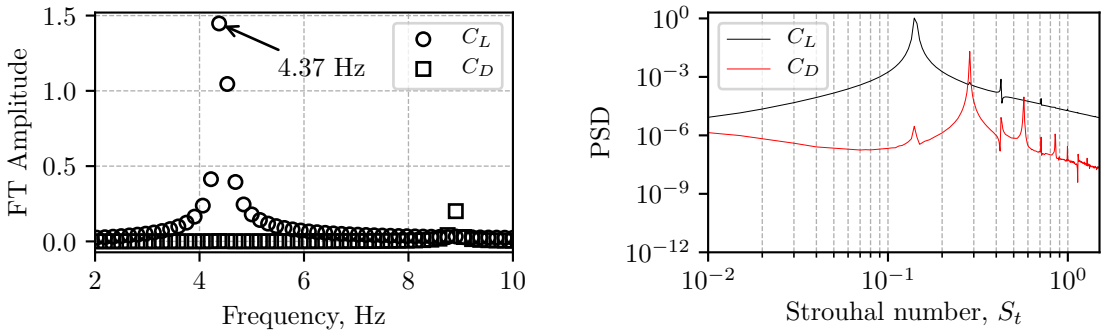

(a) SA

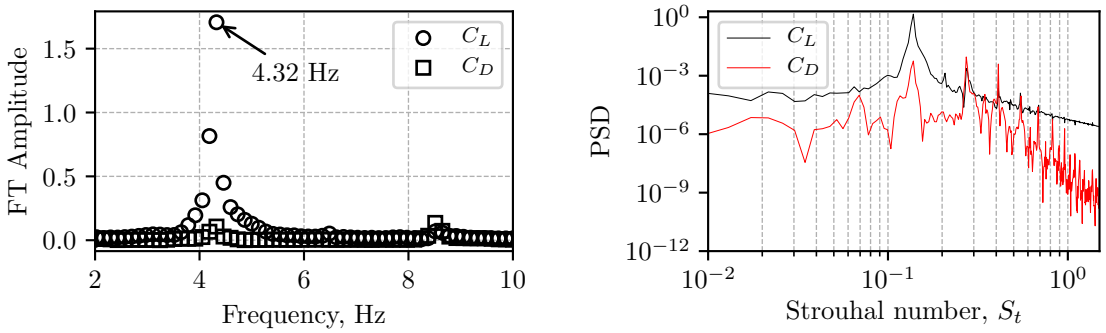

(b) k-ω SST

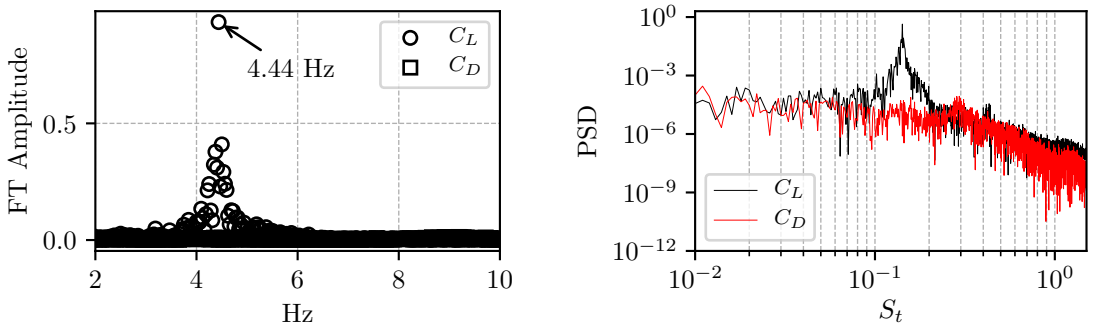

(c) DDES

Fig. 6 Time-history of force coefficients from all three solutions in the frequency and log-log power spectra domains.

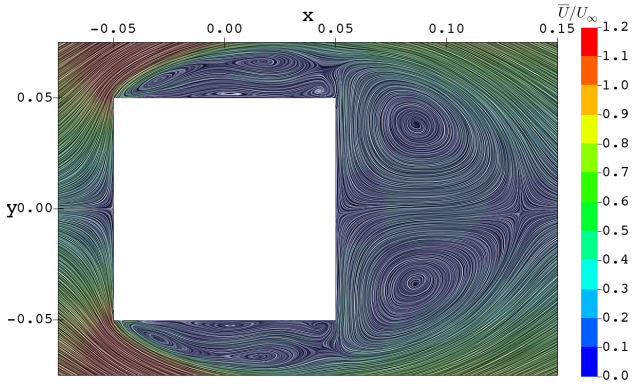

Fig. 7 Surface line integral convolution of time-averaged velocity (surface streak-lines) from the DDES case. The mean recirculation zone can be clearly seen downstream.

Table 4 Comparison of key vortex shedding parameters.

Case	Type	$Re \times 10^3$	AR	$\overline{C_D}$	S_t	λ^*	$C_D{}'$	$C_L{}'$
Present study								
SB	URANS / SA-noft2	21.4	7	2.15	0.140	0.93	0.15	1.39
	URANS / k-ω SST	21.4	7	2.26	0.138	0.93	0.16	1.44
	DDES / SA	21.4	7	2.19	0.142	1.31	0.12	0.95
	DDES / SA†	21.4	7	2.22	0.142	-	0.08	0.99
Numerical								
Boudreau et al. [16]	URANS	21.4	7	2.11	0.133	0.97	0.14	1.56
	DDES	21.4	7	2.41	0.126	1.07	0.17	1.47
Barone and Roy [28]	DES, corrected‡	19.4	4	2.11	0.125	1.42	0.26	1.16
Fureby et al. [18]	LES	21.4	8	2.1	0.131	1.25	0.17	1.30
Sohankar et al. [17]	LES, corrected	22.0	4	2.09	0.128	1.07	0.27	1.40
Minguez et al. [20]	LES, corrected	21.4	-	2.2	0.141	1.28	-	-
Trias et al. [21]	DNS	22.0	4	2.18	0.132	1.04	0.205	1.71
Experimental								
Lyn et al. [8]	Laser-Doppler	21.4	9.75	2.1	0.132	1.38	-	-
Minguez et al. [20]	Laser-Doppler	21.4	20	2.1	0.130	-	-	-
Luo et al. [40]	Water tunnel, corrected	34.0	9.2	2.21	0.13	-	0.18	1.21

* Present results are taken at the closest approximate zero-velocity discrete point.
† Results from a subsequent time-step sensitivity study.
‡ Corrected, with blockage corrections.

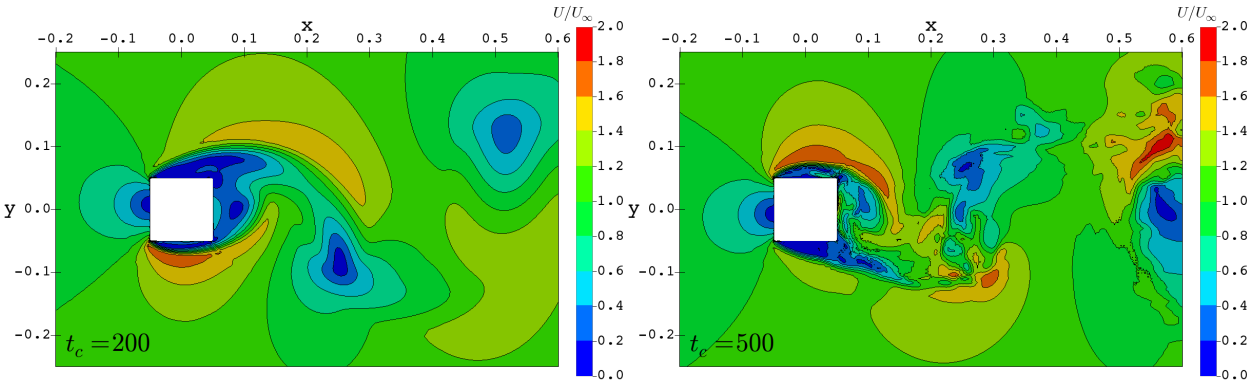

(a) URANS (SA) **(b) DDES**

Fig. 8 Instantaneous normalised velocity contours at their respective convective time-steps.

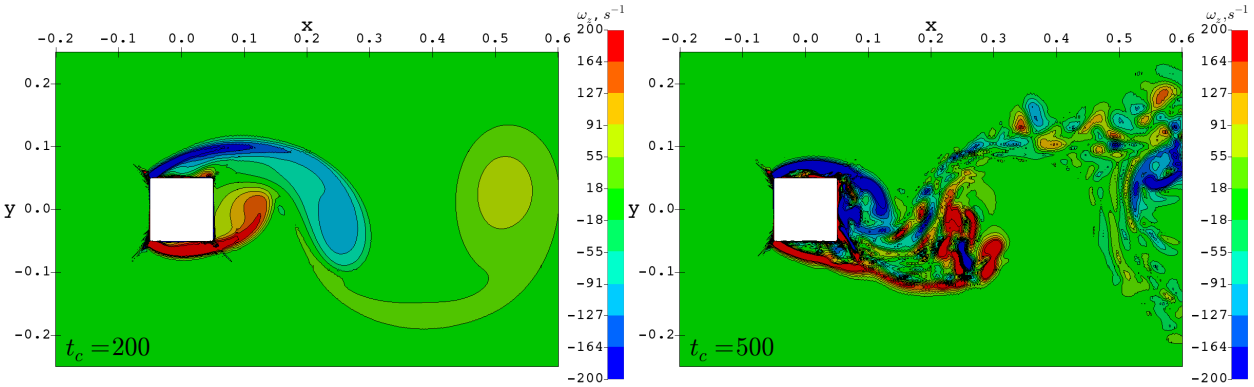

(a) URANS (SA) **(b) DDES**

Fig. 9 Instantaneous span-wise vorticity (ω_z) contours at their respective convective time-steps.

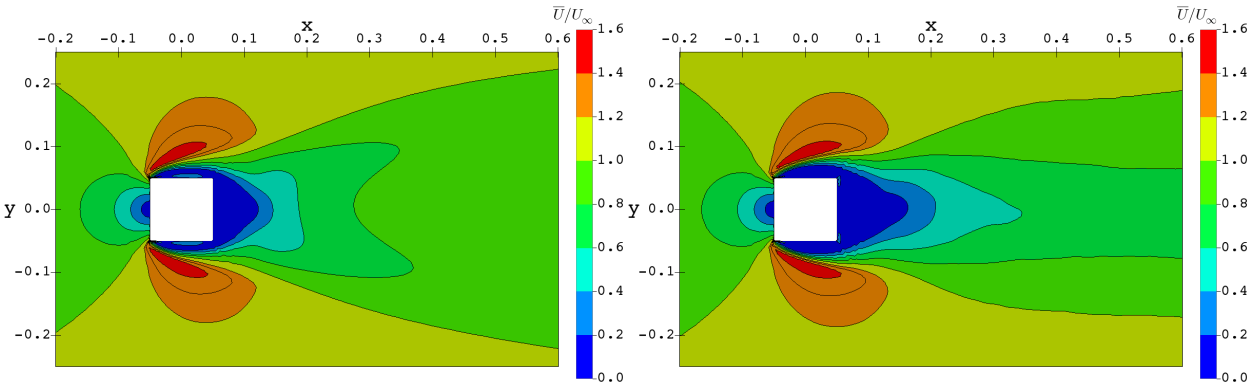

(a) URANS (SA) **(b) DDES**

Fig. 10 Time-averaged freestream-normalised velocity contours.

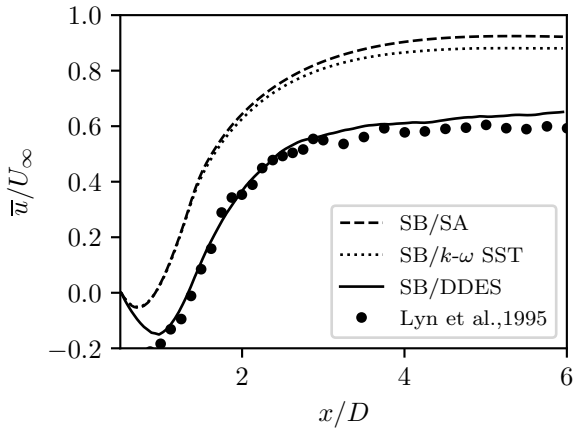

Fig. 11 Comparison of first-moment (time-averaged) statistics of both u-velocity component with experimental data [8].

entire turbulence spectrum such that only the mean flow statistics remain is therefore very apparent (Figs. 8a and 9a). Furthermore, time-averaging the velocity fields—which also appear identical for the two URANS models—also reveal a larger, diffused wake (Fig. 10). However, the vertical extent of the shear layer emanated from the leading edges are similar between both the URANS and DDES solutions, which extends to a width of approximately $2y/D$. The time-averaged velocity fields also reveal an earlier recovery in the SA solution (Fig. 10a) by almost $0.3\overline{U}/U_\infty$.

The accuracy for the first-moments of the wake capture is evaluated in terms of its wake velocity recovery along the centre, and wake profiles evaluated across 4 downstream stations. The normalised time-averaged stream-wise velocity profile is presented in Fig. 11 and evaluated against experimental data [8] up to $6x/D$. The URANS models over-predict this velocity profile, characterised as an early recovery. On the other hand, the DDES model provides excellent accuracy although marginally over-predicting beyond $3x/D$. The second-moment statistics of velocity fluctuation is evaluated along this same centre. Figure 12 illustrates the freestream-normalised root-mean-square of stream-wise, $RMS(u')/U_\infty$, and transversal $RMS(v')/U_\infty$ velocities, up to the same downstream distance of $6x/D$.

The results obtained from the URANS models generally under-predict fluctuations. However, the horizontal location of the fluctuation peak is predicted with reasonable accuracy, positioned at $x/D \approx 1.5$. Thereafter, the fluctuations depict severely damped results in the RMS of the velocity farther downstream, that plateau along $u'/U_\infty \approx 0.03$ at distances beyond $x/D = 4$ especially for the SA case. This is non-physical compared to the experimental results [8], and that observed from the DDES case. In contrast, DDES only models the turbulence spectrum partially, which are filtered based on the smallest grid scales. Investigating the total effective viscosity $(\nu + \nu_t)$ of the instantaneous field reveals a significant over-prediction in turbulent viscosity ratio, by approximately 50 times of that for the URANS cases compared to DDES which showed only a time-averaged maximum of $\nu_t/\nu = 8$ compared to 200 shown in Fig. 13. The same order of magnitude in this over-prediction of total effective viscosities is also reported [16]. In contrast to the experimental data, the DDES results predicts the fluctuation peak slightly farther downstream. This disagrees with that reported by [21], where the peak is depicted to be farther upstream instead. The fluctuations are slightly over-predicted in the near wake ($2x/D$) while it is expected for results to fall short due to damping from sub-grid scale viscosity. This observation is also highlighted by other numerical work listed in Table 4. Regardless, excellent agreement is obtained farther downstream, especially within $3 < x/D < 6$ which predicts the range of $rms(u')/U_\infty \approx 0.3$ against the experimental data [8]. The transversal fluctuations (Fig. 12b) yield similar results among the numerical cases within the $x/D < 3$ range, but begin to deviate past this distance as the URANS results begin to over-predict relative to the experimental data while the DDES solution maintains some degree of accuracy $(rms(u')/U_\infty \approx 0.1)$ for the remainder of the results.

Velocity deficit profiles for the normalized stream-wise velocity component are illustrated in Fig. 14 for $x/D = [1, 2, 3, 6]$. DDES results show excellent agreement with the experimental data at x/D, especially for the limits of the wake width at approximately $\overline{u}/U_\infty$. However, results for comparison at the farther downstream stations are unreported. Nevertheless, the wake center velocities in Fig. 11 correspond to those along the wake center in Fig. 14, and therefore confidence for the accuracy in the maximum wake momentum deficit is high. As expected for the URANS results, the

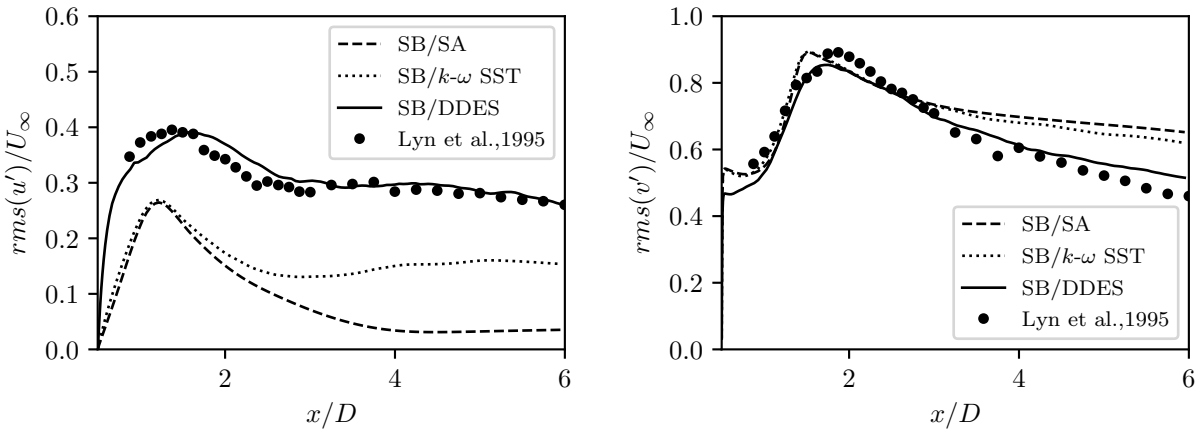

(a) u-component fluctuation. **(b) v-component fluctuation.**

Fig. 12 Comparison of second-moment (root-mean-square) statistics of u- and v-velocity component fluctuations with experimental data [8].

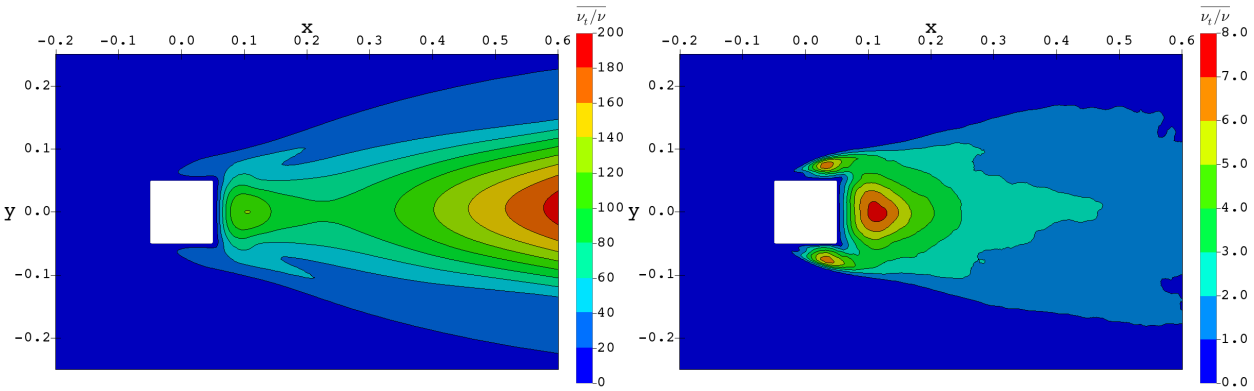

(a) URANS (SA) **(b) DDES**

Fig. 13 A significant inflation in the time-averaged turbulent viscosity ratios in the URANS solution compared to the DDES. Note the difference in scale.

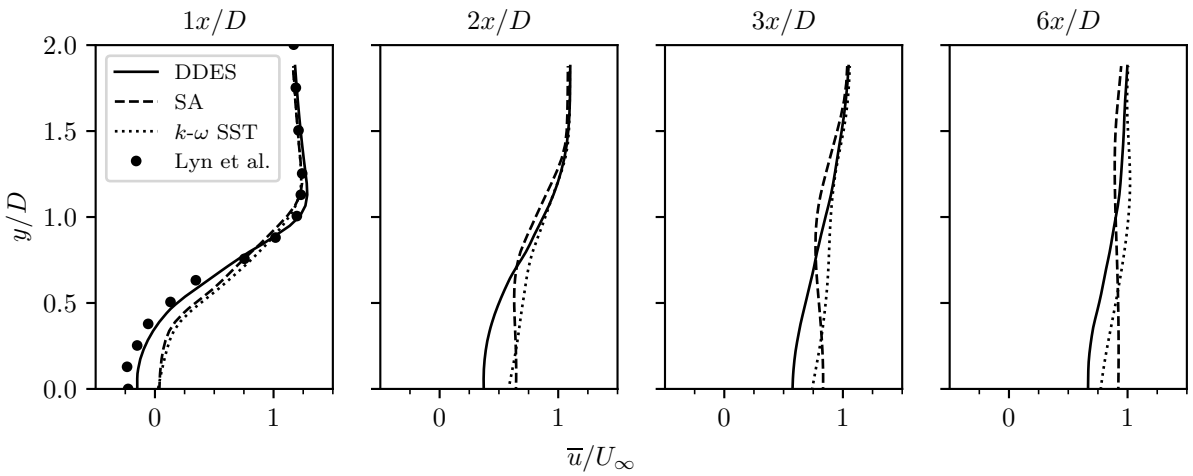

Fig. 14 Symmetrical time-averaged wake velocity profiles across subsequent downstream stations with the experiment data [8].

wake velocity profiles model early wake recovery farther downstream and prove to be inadequate at capturing even the first-moment statistics along this location.

The results obtained so far has demonstrated good correlation in terms of the wake descriptors and also quantitatively for vortex shedding parameters against the cited sources. Key vortex structures were also identified, illustrating different orders of fidelty across the two tested turbulence modelling methods. These have good accuracy and are comparable even to that of LES and DNS methods [17, 21] among others, despite being conducted on an identical grid with the RANS models.

IV. Concluding Remarks

Statistical and instantaneous results of vortex shedding and wake capture for a massively separated flow generated by a bluff-body are provided with URANS and DDES methods obtained on identical grids. The solutions presented are nominally second-order accurate using an implicit constant backward time-stepping scheme coupled with a blended upwind-central differencing spatial discretization scheme. Shedding dynamics, including the Strouhal number, statistics of lift and drag coefficients, along with time-averaged moment statistics of the wake profiles and stresses are among the results presented. Although the Strouhal number is slightly over-predicted compared to experimental values, the effects of blockage and the application of correction factors need to be considered when imposing the appropriate far-field boundary conditions as this will influence the resulting shedding frequencies. Additionally, this dominant frequency was insensitive to time-discretization studies with half a time-step size. Key vortex structures were also identified among the models tested, and the von Kármán sheet was identified of varying resolution based on the turbulence model used. The amount of detail in the flow were also reflected in the respective force coefficient spectra, which showed good correlation with existing sources for the dominant wake shedding frequencies.

For wake capture, the errors for URANS are attributed to inherent damping, evident as as inflation in total effective viscosity that affects even the mean flow. The DDES results in comparison, demonstrate excellent accuracy that is even comparable to that of LES [17, 20] and DNS [21] methods for wake recovery and RMS statistics up to the measured distance of $6x/D$ compared against experimental data [8]. This supersedes RANS in terms of accuracy on the given (RANS-calibrated) grid resolution ($\Delta = 0.05D$), and the significant improvement in accuracy is achieved with just a marginal trade-off in computational effort that is still much lower than that required of LES. The present work contributes as an additional reference for future cases involving the modeling and verification of bluff-body wake capture. Based on the results conducted under the present conditions, the outlined approach expands on the best practices for wake capture and assessment, considering the robustness of accuracy and computational economy for DDES among the hierarchy of turbulence modeling techniques. This applies especially for practical applications, where the importance accurate capture precedes its interaction with downstream bodies for aerodynamic loads.

Acknowledgments

The work is funded through the Industrial Postgraduate Programme scholarship by the Economic Development Board of Singapore, in partnership between AviationLearn Pte. Ltd. and the University of Glasgow Singapore.

References

[1] Cowan, I. R., Castro, I. P., and Robins, A. G., "Numerical Considerations for Simulations of Flow and Dispersion Around Buildings," *Journal of Wind Engineering and Industrial Aerodynamics*, Vol. 67, 1997, pp. 535–545.

[2] Forrest, J. S., Owen, I., Padfield, G. D., and Hodge, S. J., "Ship-Helicopter Operating Limits Prediction Using Piloted Flight Simulation and Time-Accurate Airwakes," *Journal of Aircraft*, Vol. 49, No. 4, 2012, pp. 1020–1031.

[3] Chirico, G., Szubert, D., Vigevano, L., and Barakos, G. N., "Numerical Modelling of the Aerodynamic Interference Between Helicopter and Ground Obstacles," *CEAS Aeronautical Journal*, Vol. 8, No. 4, 2017, pp. 589–611.

[4] Raza, S. A., and Etele, J., "Autonomous Position Control Analysis of Quadrotor Flight in Urban Wind Gust Conditions," *AIAA Guidance, Navigation, and Control Conference*, 2016, p. 1385.

[5] Van Muijden, J., Boelens, O., van der Vorst, J., and Gooden, J., "Computational Ship Airwake Determination to Support Helicopter-Ship Dynamic Interface Assessment," *21st AIAA Computational Fluid Dynamics Conference*, 2013, p. 3078.

[6] Galway, D., Etele, J., and Fusina, G., "Development and Implementation of an Urban Wind Field Database for Aircraft Flight Simulation," *Journal of Wind Engineering and Industrial Aerodynamics*, Vol. 103, 2012, pp. 73–85.

[7] "European Research Community on Flow, Turbulence, and Combustion Database," Available at `http://cfd.mace.manchester.ac.uk/ercoftac/index.html`, 2020. 2020-04-20.

[8] Lyn, D., Einav, S., Rodi, W., and Park, J.-H., "A Laser-Doppler Velocimetry Study of Ensemble-Averaged Characteristics of the Turbulent Near Wake of a Square Cylinder," *Journal of Fluid Mechanics*, Vol. 304, 1995, pp. 285–319.

[9] Bai, H., and Alam, M. M., "Dependence of Square Cylinder Wake on Reynolds Number," *Physics of Fluids*, Vol. 30, No. 1, 2018, p. 015102.

[10] Jiang, H., and Cheng, L., "Flow Separation Around a Square Cylinder at Low to Moderate Reynolds Numbers," *Physics of Fluids*, Vol. 32, No. 4, 2020, p. 044103.

[11] Jiang, H., Cheng, L., and An, H., "Three-Dimensional Wake Transition of a Square Cylinder," *Journal of Fluid Mechanics*, Vol. 842, 2018, pp. 102–127.

[12] Jiang, H., and Cheng, L., "Hydrodynamic Characteristics of Flow Past a Square Cylinder at Moderate Reynolds Numbers," *Physics of Fluids*, Vol. 30, No. 10, 2018, p. 104107.

[13] Mahon, S., and Zhang, X., "Computational Analysis of Pressure and Wake Characteristics of an Aerofoil in Ground Effect," *Journal of Fluids Engineering*, Vol. 127, No. 2, 2005, p. 290.

[14] Rumsey, C., "NASA LaRC, Turbulence Modelling Resource," Available at `https://turbmodels.larc.nasa.gov/`, 2017. 2018-08-15.

[15] Wang, Y. Q., "Effects of Reynolds number on Vortex Structure Behind a Surface-Mounted Finite Square Cylinder with AR= 7," *Physics of Fluids*, Vol. 31, No. 11, 2019, p. 115103.

[16] Boudreau, M., Dumas, G., and Veilleux, J.-C., "Assessing the Ability of the DDES Turbulence Modeling Approach to Simulate the Wake of a Bluff Body," *Aerospace*, Vol. 4, No. 3, 2017, p. 41.

[17] Sohankar, A., Davidson, L., and Norberg, C., "Large Eddy Simulation of Flow Past a Square Cylinder: Comparison of Different Subgrid Scale Models," *Journal of Fluids Engineering*, Vol. 122, No. 1, 2000, pp. 39–47.

[18] Fureby, C., Tabor, G., Weller, H., and Gosman, A., "Large Eddy Simulations of the Flow Around a Square Prism," *AIAA Journal*, Vol. 38, No. 3, 2000, pp. 442–452.

[19] Uffinger, T., Ali, I., and Becker, S., "Experimental and Numerical Investigations of the Flow Around Three Different Wall-Mounted Cylinder Geometries of Finite Length," *Journal of Wind Engineering and Industrial Aerodynamics*, Vol. 119, 2013, pp. 13–27.

[20] Minguez, M., Brun, C., Pasquetti, R., and Serre, E., "Experimental and High-Order LES Analysis of the Flow in Near-Wall Region of a Square Cylinder," *International Journal of Heat and Fluid Flow*, Vol. 32, No. 3, 2011, pp. 558–566.

[21] Trias, F., Gorobets, A., and Oliva, A., "Turbulent Flow Around a Square Cylinder at Reynolds Number 22,000: A DNS study," *Computers & Fluids*, Vol. 123, 2015, pp. 87–98.

[22] Yarusevych, S., and H. Boutilier, M. S., "Vortex Shedding of an Airfoil at Low Reynolds Numbers," *AIAA Journal*, Vol. 49, No. 10, 2011, pp. 2221–2227.

[23] Huang, R. F., and Lin, C. L., "Vortex Shedding and Shear-Layer Instability of Wing at Low-Reynolds Numbers," *AIAA Journal*, Vol. 33, No. 8, 1995, pp. 1398–1403.

[24] Lienhard, J. H., *Synopsis of Lift, Drag, and Vortex Frequency Data for Rigid Circular Cylinders*, Vol. 300, Technical Extension Service, Washington State University, 1966.

[25] Spalart, P. R., "Comments on the Feasibility of LES for Wings, and on a Hybrid RANS/LES Approach," *Proceedings of First AFOSR International Conference on DNS/LES*, Greyden Press, 1997.

[26] Spalart, P. R., Deck, S., Shur, M. L., Squires, K. D., Strelets, M. K., and Travin, A., "A New Version of Detached-Eddy Simulation, Resistant to Ambiguous Grid Densities," *Theoretical and Computational Fluid Dynamics*, Vol. 20, No. 3, 2006, p. 181.

[27] Strelets, M., "Detached Eddy Simulation of Massively Separated Flows," *39th Aerospace Sciences Meeting and Exhibit*, 2001, p. 879.

[28] Roy, C. J., and Barone, M. F., "Evaluation of Detached Eddy Simulation for Turbulent Wake Applications," Tech. rep., Sandia National Laboratories, 2005.

[29] Spalding, D. B., "A Novel Finite Difference Formulation for Differential Expressions Involving Both First and Second Derivatives," *International Journal for Numerical Methods in Engineering*, Vol. 4, No. 4, 1972, pp. 551–559.

[30] Lee, S. B., "A Study on Temporal Accuracy of OpenFOAM," *International Journal of Naval Architecture and Ocean Engineering*, Vol. 9, No. 4, 2017, pp. 429–438.

[31] Courant, R., Friedrichs, K., and Lewy, H., "On the Partial Difference Equations of Mathematical Physics," *IBM Journal of Research and Development*, Vol. 11, No. 2, 1967, pp. 215–234.

[32] Spalart, P., and Allmaras, S., "A One-Equation Turbulence Model for Aerodynamic Flows," *30th Aerospace Sciences Meeting and Exhibit*, 1992, p. 439.

[33] Allmaras, S. R., and Johnson, F. T., "Modifications and Clarifications for the Implementation of the Spalart-Allmaras Turbulence Model," *Seventh International Conference on Computational Fluid Dynamics (ICCFD7)*, 2012, pp. 1–11.

[34] Menter, F. R., "Performance of Popular Turbulence Model for Attached and Separated Adverse Pressure Gradient Flows," *AIAA Journal*, Vol. 30, No. 8, 1992, pp. 2066–2072.

[35] Shih, T.-H., Liou, W. W., Shabbir, A., Yang, Z., and Zhu, J., "A New Eddy Viscosity Model for High Reynolds Number Turbulent Flows," *Computers & Fluids*, Vol. 24, No. 3, 1995, pp. 227–238.

[36] Jasak, H., Jemcov, A., Tukovic, Z., et al., "OpenFOAM: A C++ Library for Complex Physics Simulations," 2007.

[37] "The OpenFOAM Foundation," Available at `https://openfoam.org/`, 2019. 2020-04-20.

[38] Von Kármán, T., "Mechanical Similitude and Turbulence," *Technical Memorandum*, 1931.

[39] Jeong, J., and Hussain, F., "On the Identification of a Vortex," *Journal of Fluid Mechanics*, Vol. 285, 1995, pp. 69–94.

[40] Luo, S., Yazdani, M. G., Chew, Y., and Lee, T., "Effects of Incidence and Afterbody Shape on Flow Past Bluff Cylinders," *Journal of Wind Engineering and Industrial Aerodynamics*, Vol. 53, No. 3, 1994, pp. 375–399.